Eur. Phys. J. Plus (2022) 137:618
https://doi.org/10.1140/epjp/s13360-022-02830-4

THE EUROPEAN PHYSICAL JOURNAL PLUS

Regular Article

Antiferromagnetic spin-1 XYZ model with the Dzyaloshinskii–Moriya interaction

Erhan Albayrak[a]

Department of Physics, Erciyes University, 38039 Kayseri, Turkey

Received: 12 April 2022 / Accepted: 16 May 2022

Abstract Antiferromagnetic spin-1 XYZ model is examined by using a mean-field approach with the introduction of spin operators on the simple cubic lattice. The model includes the crystal field interaction (D_z) along the z-axis, the Dzyaloshinskii–Moriya interaction (Δ_m) and an external magnetic field with the components of $H_x = H_y = H_z = H$. The bilinear exchange interaction parameter (J_z) is taken as a scaling parameter chosen to be negative to simulate the antiferromagnetic interactions between the nearest-neighbor spins. Thermal variations of the total magnetization and its components are investigated in detail to obtain the phase diagrams on the $(H/|J_z|, T/|J_z|)$, $(D_z/|J_z|, T/|J_z|)$ and $(\Delta_m/|J_z|, T/|J_z|)$ planes. The model exhibits antiferromagnetic, paramagnetic and random phase regions. Very interesting various phase lines and critical points are observed including the tricritical points, bicritical points, critical end points and two more. The reentrant behavior is also observed for appropriate values of the system parameters.

1 Introduction

Antiferromagnetic materials demonstrate a special demeanor in an applied magnetic field depending on the temperature. The material shows no response to the external magnetic field at very low temperatures, since the antiparallel ordering of atoms is strictly maintained. Some atoms break free of the antiparallel arrangement and align with the external magnetic field at higher temperatures. This alignment remains until a critical temperature called as the Néel temperature [1]. Above this temperature, thermal agitation progressively prevents alignment of the atoms with the magnetic field, so that the weak magnetism produced in the material by the alignment of its atoms continuously decreases as temperature is increased.

In addition, when the spins are chosen to lie along a given axis, which is usually taken as the z-axis, the problem is relatively easier in comparison with the two- or three-dimensional cases. The latter leads to the quantum spin models which is much more difficult and may be approached by using the Schrödinger equations or Heisenberg models. The difficulty arises from the nonlinearity of the considered equations [2–7] in addition to the non-commutativity of the spin operators.

Some examples for the two-dimensional models usually include the bilinear interaction parameter in the z-direction and the transverse magnetic field in the x-direction which were considered in the effective-field theory (EFT) [8–13]. Besides, some other parameters were also included in this model, such as the addition of the longitudinal crystal field in the EFT [14], the longitudinal magnetic field by combining the pair approximation with the discretized path-integral representation [15], random longitudinal crystal-field interactions in terms of an expansion technique for cluster identities of localized spin systems [16], the longitudinal crystal and external magnetic fields [17] and the effect of random transverse crystal field [18] in terms of a mean-field approximation (MFA), the Blume–Capel (BC) model with longitudinal random crystal and transverse magnetic fields in the MFA [19,20] and with both transverse field and transverse crystal field in a stochastic series expansion quantum Monte Carlo method [21]. The Blume–Emery–Griffiths (BEG) model was also used by including the transverse fields effects [22] in the MFA, the random transverse field with the EFT [23] and a new effective correlation MFA in a transverse crystal field [24]. The Oguchi approximation (OA) was also considered in a few works. The spin-1/2 anisotropic Heisenberg model was studied by taking into account the Dzyaloshinskii–Moriya (DM) interaction parameter [25] and by the consideration of the second-nearest-neighbor exchange interactions [26]. Both exchange interaction and single-ion anisotropy effects were examined in the mixed spin-1 and spin-1/2 case [27], its compensation temperature behavior [28] and the investigation of magnetic susceptibility [29], in the mixed spin-3/2 and spin-1/2 model [30] and with random crystal field [31] and, in the mixed spin-2 and spin-1/2 for the square [32] and simple cubic lattices [33].

The DM interaction is an antisymmetric exchange interaction with a contribution to total magnetic exchange interaction between two neighboring magnetic spins as a source of weak ferromagnetic behavior in an antiferromagnet. The spin-1/2 model with the inclusion of the DM interaction (DMI) was established in a precise mapping correspondence to the simple spin-1/2 Ising model on Kagome lattice [34], in the EFT with the study of the critical and reentrant behaviors for the antiferromagnet model in a longitudinal magnetic field [35], the MFA in the study of the potassium jarosite compound $KFe_3(OH)_6(SO_4)_2$ for the antiferromagnetic XY

[a] e-mail: albayrak@erciyes.edu.tr (corresponding author)

Published online: 23 May 2022

model [36], in the matrix-product-state method to examine the quantum phase transitions and the ground-state phase diagram for the Heisenberg–Ising alternating chain [37], the magnetization of triangular-lattice antiferromagnets $Ba_3CoSb_2O_9$ and $CsCuCl_3$ with a 120° spin structure in the ab plane [38], in a combined analytical and density matrix renormalized group study of the antiferromagnetic XXZ chain in a transverse magnetic field [39], the pair XYZ Heisenberg interaction and quartic Ising interactions was exactly solved by establishing a precise mapping relationship with the corresponding zero-field eight-vertex model [40] and with antiferromagnetic exchange interactions in the presence of a longitudinal external magnetic field by employing the usual MFA [41].

In order to see the effects of crystal field on this system, the spin-1 models were also taken under consideration. A few examples may be given as: the two-spin cluster MF method on the simple cubic lattice [42], the Schwinger boson MF theory for one-dimensional antiferromagnet [43], the infinite time-evolving block decimation method on ground-state phase diagrams of alternating chains [44], the local moments on the pyrochlore lattice with a generic interacting spin model on a pyrochlore lattice [45], the chain in the presence of an external magnetic field by using a combination of numerical and analytical techniques [46] and the two-dimensional Heisenberg model with Ising anisotropy and dipolar interaction under zero and finite magnetic fields using a Monte Carlo method [47]. The quantum-memory-assisted entropic uncertainty relations in two-qutrit spin-1 Heisenberg XYZ and XXX chains under homogeneous magnetic fields were studied [48]. The spin-1 SU(3)-models in the seven-parameter manifold of translation- and reflection-invariant Hamiltonians with nearest-neighbor couplings were considered [49]. The quantum coherence was studied in a spin chain with both symmetric exchange and antisymmetric DM couplings [50]. The XYZ Heisenberg model was considered from the standpoint of the quantum inverse problem method [51]. The negativity as a measure of thermal entanglement was studied for a two-qutrit spin-1 anisotropic Heisenberg XYZ chain with the DM interaction in a homogeneous magnetic field [52]. As we can see from these works, the thermal variations and the DMI effects on the magnetization and magnetic phase diagrams have not been considered in detail.

Recently, the spin-1 XYZ model with the DMI effects was examined in the MFA by introducing the spin operators for the ferromagnetic case, i.e., $J_z > 0.0$ [53] and very interesting behaviors for the magnetization and phase diagrams were observed. In this work, the antiferromagnetic case with $J_z < 0.0$ is considered for the Hamiltonian consisting of the DMI parameter Δ_m, the crystal field D_z along the z-axis and the external magnetic field in all three dimensions with $H_x = H_y = H_z = H$ for the coordination number $q = 6.0$ corresponding to the simple cubic lattice. The thermal variations of the total magnetization and its components are investigated in detail to obtain the phase diagrams on the $(H/|J_z|, T/|J_z|)$, $(D_z/|J_z|, T/|J_z|)$ and $(\Delta_m/|J_z|, T/J_z)$ planes for given values Δ_m, D_z and H.

The remainder of this work is structured as follows: Sect. 2 involves our approach to the formulation in the MFA, the thermal variations of net magnetization are illustrated in Sect. 3, Sect. 4 contains the phase diagrams, and the last section includes a brief summary and conclusions.

2 The formulation

The spin-1 XYZ model Heisenberg Hamiltonian in terms of the bilinear exchange interaction parameter (J_z) between the nearest-neighbor (NN) spins, the crystal field (D_z) along the z-axis, the DMI (Δ_m) and external magnetic field components (H_x, H_y, H_z) is given as:

$$\begin{aligned}\mathcal{H} = &-J_z \sum_{\langle i,j\rangle} S_i^z S_j^z - \sum_i D_z \left(S_i^z\right)^2 - \Delta_m \sum_{\langle i,j\rangle} \left(S_i^x S_j^y - S_i^y S_j^x\right) \\ &-H_x \sum_i S_i^x - H_y \sum_i S_i^y - H_z \sum_i S_i^z,\end{aligned} \tag{1}$$

where $\langle i, j\rangle$ points out the summation over the NN spins, $J_z < 0$ for the antiferromagnetic (AFM) interaction and S_i^x, S_i^y and S_i^z are the components of spin-1 operator at site i which are presented in the matrix forms as:

$$S_i^x = \frac{1}{\sqrt{2}}\begin{pmatrix}0 & 1 & 0\\ 1 & 0 & 1\\ 0 & 1 & 0\end{pmatrix}, \quad S_i^y = \frac{1}{\sqrt{2}}\begin{pmatrix}0 & -i & 0\\ i & 0 & -i\\ 0 & i & 0\end{pmatrix}, \quad S_i^z = \begin{pmatrix}1 & 0 & 0\\ 0 & 0 & 0\\ 0 & 0 & -1\end{pmatrix}. \tag{2}$$

In order to surmount the difficulty of studying the quantum mechanical model, we approach to the problem by using a mean-field approximation. Even if this approach does not lead to the exact solutions, one can get at least some qualitative results. Therefore, the Hamiltonian $\mathcal{H}$ in Eq. (1) can be written in the MF form as:

$$-\beta\mathcal{H}_{\mathrm{MFA}} = -\beta \sum_i \mathcal{H}_{\mathrm{MFA}}^{(i)} \tag{3}$$

in which

$$-\beta\mathcal{H}_{\mathrm{MFA}}^{(i)} = \beta q J_z M_z S_i^z + \beta D_z \left(S_i^z\right)^2 + \beta q \Delta_m \left(M_y S_i^x - M_x S_i^y\right) + \beta \left(H_x S_i^x + H_y S_i^y + H_z S_i^z\right) \tag{4}$$

where $M_\mu = \langle S_j^\mu \rangle$ are the magnetization components with $\mu = x, y, z$, $\beta = 1/(kT)$, k is being the Boltzmann constant and set to 1.0 for convenience and q is the number of the NNs.

The matrix representation of $-\beta\mathcal{H}_{\mathrm{MFA}}^{(i)}$ is achieved by using the spin operators, i.e., Eq. (2), and found as:

$$-\beta\mathcal{H}_{\mathrm{MFA}}^{(i)} = \begin{pmatrix} \beta(D_z + H_z + q J_z M_z) & H_{12} & 0 \\ H_{21} & 0 & H_{23} \\ 0 & H_{32} & \beta(D_z - H_z - q J_z M_z) \end{pmatrix} \tag{5}$$

in which $H_{12} = H_{23} = \frac{\beta}{\sqrt{2}}[(H_x - iH_y) + q\Delta_m(iM_x + My)]$ and $H_{32} = H_{21} = H_{12}^* = H_{23}^*$, i.e., the last two are the complex conjugates of first two. The eigenvalues of this matrix are real and are attained from the below third degree equation

$$\lambda^3 + a_2\lambda^2 + a_1\lambda + a_0 = 0 \tag{6}$$

where the coefficients are found as:

$$\begin{aligned} a_0 &= \beta^3 D_z \left[H_x^2 + H_y^2 + 2q\Delta_m(H_x M_y - H_y M_x) + q^2\Delta_m^2\left(M_x^2 + M_y^2\right)\right], \\ a_1 &= \beta^2 \left[D_z^2 - H_x^2 - H_y^2 - H_z^2 + 2q\Delta_m(H_y M_x - H_x M_y) - 2q H_z J_z M_z \right. \\ &\quad \left. -q^2\Delta_m^2\left(M_x^2 - M_y^2\right) - q^2 J_z^2 M_z^2\right], \\ a_2 &= -2\beta D_z. \end{aligned} \tag{7}$$

The eigenvalues are reached by using the mathematical identity given as:

$$\lambda_{n+1} = 2y\cos\left[\frac{1}{3}\left\{\arccos\left(-\frac{G}{2y^3}\right) + 2n\pi\right\}\right] - \frac{a_2}{3}, \qquad n = 0, 1, 2. \tag{8}$$

with $y = (-W)^{1/2}$, $W = (3a_1 - a_2^2)/9$ and $G = (27a_0 - 9a_1a_2 + 2a_2^3)/27$.

The partition function can be calculated by using these three eigenvalues obtained from the MFA Hamiltonian as:

$$\begin{aligned} Z_i &= \mathrm{Tr}_{(i)} \exp\left[-\beta\mathcal{H}_{\mathrm{MFA}}^{(i)}\right] \\ &= \sum_{n=1}^{3} e^{\lambda_n} = e^{\lambda_1} + e^{\lambda_2} + e^{\lambda_3}. \end{aligned} \tag{9}$$

The free energy of the model is found from the well-known definition by the usage of the partition function as:

$$f = -\frac{1}{\beta}\ln Z_i \tag{10}$$

which will be utilized to find the formulations of the order-parameters. The dipolar moments or magnetization components, $M_\mu = \langle S_j^\mu \rangle$ with $\mu = x, y, z$ are found from

$$\begin{aligned} M_\mu = \langle S_i^\mu \rangle &= -\frac{\partial f}{\partial H_\mu} = \frac{1}{\beta}\frac{\partial \ln Z_i}{\partial H_\mu} = \frac{\mathrm{Tr}_{(i)}\left[S_i^z \exp\left(-\beta\mathcal{H}_{\mathrm{MFA}}^{(i)}\right)\right]}{Z_i} \\ &= \frac{1}{\beta}\left[\frac{\frac{\partial\lambda_1}{\partial H_\mu}e^{\lambda_1} + \frac{\partial\lambda_2}{\partial H_\mu}e^{\lambda_2} + \frac{\partial\lambda_3}{\partial H_\mu}e^{\lambda_3}}{e^{\lambda_1} + e^{\lambda_2} + e^{\lambda_3}}\right] \\ &= \frac{1}{\beta'}\left[\frac{\frac{\partial\lambda_1}{\partial h_\mu}e^{\lambda_1} + \frac{\partial\lambda_2}{\partial h_\mu}e^{\lambda_2} + \frac{\partial\lambda_3}{\partial h_\mu}e^{\lambda_3}}{e^{\lambda_1} + e^{\lambda_2} + e^{\lambda_3}}\right]. \end{aligned} \tag{11}$$

where $\beta' = \beta J_z$ and $h_\mu = H_\mu/J_z$ which are the reduced temperature and external magnetic field components.

It should be noted that the lattice must be divided into two sublattices A and B to count the AFM interactions, i.e., $J_z < 0.0$. Thus, the magnetization components for the sublattices must be written as:

$$\begin{aligned} M_\mu^A &= M_\mu^A\left(M_x^B, M_y^B, M_z^B\right), \\ M_\mu^B &= M_\mu^B\left(M_x^A, M_y^A, M_z^A\right). \end{aligned} \tag{12}$$

Since the magnetization vector is given as $\vec{M} = M_x\hat{i} + M_y\hat{j} + M_z\hat{k}$, the sublattice magnetizations can be obtained from

$$M_A = \sqrt{\sum_{\delta=x,y,z} \left(M_\mu^A\right)^2} = \sqrt{\left(M_x^A\right)^2 + \left(M_y^A\right)^2 + \left(M_z^A\right)^2} \tag{13}$$

and

$$M_B = \sqrt{\sum_{\delta=x,y,z} \left(M_\mu^B\right)^2} = \sqrt{\left(M_x^B\right)^2 + \left(M_y^B\right)^2 + \left(M_z^B\right)^2}. \tag{14}$$

Finally, the total magnetization of the system, i.e., the net magnetization, is given as:

$$M_{\text{Tot}} = M_A - M_B. \tag{15}$$

After having calculated the magnetization components and net magnetization for the sublattices A and B, we are now ready to study their thermal variations for given values of D_z, Δ_m, the external magnetic field components chosen as $H = H_x = H_y = H_z$ and the coordination number $q = 6$ corresponding to the simple cubic lattice. An iterative procedure is followed for the calculation of our order-parameters with given values of the system parameters under temperature variations. The obtained results are presented in the next section.

3 Thermal variations of net magnetization

The usual approach to obtain the phase diagrams involves the study of thermal changes of magnetization. It is well known that when magnetization goes to zero continuously, it is called as the second-order phase transition (SOPT), and when it presents a discontinuity, it is the first-order phase transition (FOPT), the lines of which enclose a region of the ordered phase, i.e., the AFM phase since $J_z < 0.0$. In addition to these phase regions, this work also reveals a region of random or oscillatory behavior for magnetization which is well confined by the borders and it is to be called as the random phase regions. The temperatures at which these phase transitions take place are denoted as T_c, T_t and T_r for the SOPT, FOPT and random cases, respectively. A model can display any combinations of these phase transitions or the same ones more than once. When the latter occurs, the reentrant behavior appears in the phase diagrams.

Before presenting the thermal variations of M_{Tot}, it should be noted we have combined together two solutions of $\pm M_{\text{Tot}}$ whenever it is possible which allows us to distinguish the symmetric and anti-symmetric solutions. In Fig. 1, the topological thermal variation plots of the total magnetization, M_{Tot}, are presented for given values of (Δ_m, H, D_z) when $q = 6$ and $J_z = -1.0$. Figure 1a and b shows the existence of one T_c, while Fig. 1c and d presents two T_c's. Figure 1e shows that the magnetization lines enclosing the AFM phase at lower temperatures, before termination they start oscillating randomly at the T_r and this randomness ends at the second T_r. Afterward, the system enters into the PM phase. Figure 1f first shows the AFM phase at lower temperatures which terminates at the T_c. Then the system enters into the PM phase. With the increasing temperature, the random phase appears at T_r which also terminate at the second T_r with the entrance of the PM phase again. It is shown in Fig. 1g that the random phase starts from zero and finishes at the T_r, then M_{Tot} separates the AFM phase which expires at the T_c. Figure 1h and i shows the existence of T_t's. The first one gives a T_t and then a T_c and the last one gives only a T_t. In Fig. 1j and k, the random phase starts at zero temperature and terminates at the T_r's. $M_{\text{Tot}} = 0.0$ appears at lower temperatures and then, the random phase starts from the first T_r with increasing temperature and disappears at the second T_r which leads to the reentrant behavior as seen in Fig. 1l. M_{Tot} shows itself in an oscillatory fashion in Fig. 1m which terminates at the T_r. When the random solutions are zoomed closer, this oscillatory behavior is observed in some cases; therefore, they are not distinguished from each other in this work. Figure 1n first shows a T_t and then two T_r's. The final plot, Fig. 1o shows a T_r then a T_t and then a T_c, i.e., all types of phase transitions coexist together.

In the next section, we combine all these solutions to construct the phase diagrams on the possible planes of our system parameters. The combinations of these points make up the possible phase lines and their combinations lead to the some critical points.

4 The phase diagrams

We are now ready to construct the phase diagrams on the $(H/|J_z|, T/|J_z|)$, $(D_z/|J_z|, T/|J_z|)$ and $(\Delta_m/|J_z|, T/|J_z|)$ planes for given values of Δ_m, H and D_z, under the conditions $H_x = H_y = H_z = H$ and $q = 6$ with J_z taken as a scaling factor. It is found that the model exhibits SOPT, FOPT and random phase lines which are denoted by the solid, dashed and dotted-dashed lines and called as T_c-, T_t- and T_r-lines, respectively. These lines can combine at some critical points in doubles or triples: It is well known that the tricritical point is the point at which the T_c- and T_t-lines merge together is called here as TCP_1 in shorthand notation. Similarly, the point at which the T_c- and T_r-lines combined together is called as TCP_2, while the meeting point of T_t- and T_r-lines is called as TCP_3. They are denoted with the solid, empty and dashed circles in the phase diagrams, respectively. The bicritical point

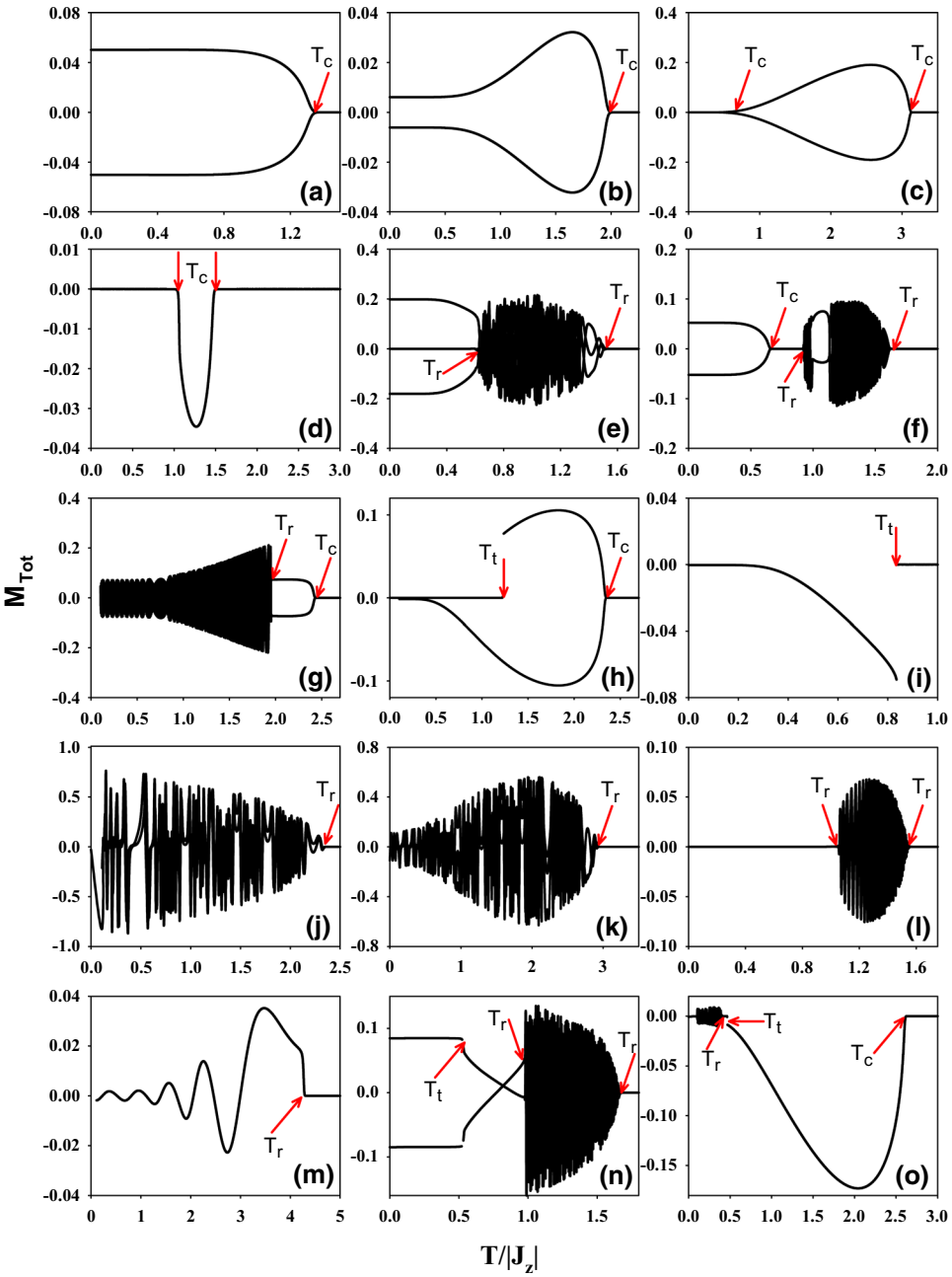

Fig. 1 Thermal variations of total magnetization for given values of (Δ_m, H, D_z) as **a** (0.6, 3.0, −2.0), **b** (0.3, 3.0, −1.0), **c** (0.75, 3.0, 0.0), **d** (1.0, 4.25, 0.5), **e** (0.77, 3.0, −3.0), **f** (1.0, 4.0, −2.8), **g** (0.5, 0.5, −2.6), **h** (0.25, 1.0, −2.5), **i** (0.25, 0.5, −3.5), **j** (0.6, 3.0, −3.0), **k** (0.94, 3.0, −2.0), **l** (1.0, 4.0, −3.1), **m** (1.0, 0.2, −2.0), **n** (1.0, 4.0, −2.25) and **o** (1.0, 4.0, 0.5)

is the combination point of two same type and one other type of phase lines. When two T_t-lines and a T_c-line, two T_r-lines and a T_c-line and two T_r-lines and a T_t-line do this called as the BCP_1, BCP_2 and BCP_3 and shown with the solid, empty and dashed squares, respectively. In addition, the critical end point is observed when a critical line is terminated on another critical line. When this happens with T_c-line ending on T_t-line, T_c-line terminating on T_r-line and T_t-line finishing on T_r-line are called as CEP_1, CEP_2 and CEP_3 and denoted with the solid, empty and dashed ellipses, respectively. In addition, the combination points of the T_c-, T_t- and T_r-lines denoted with a star. The final type of critical point observed in this work is termination of the T_c- and T_t-lines on the line of T_r-line denoted with a cross.

Before the presentations of phase diagrams, the possible effects of our system parameters should be mentioned briefly. As D_z gets low negative enough the lowest spin value, i.e., the zero state of spin-1, is preferred. External magnetic field tries to align the spins in the given direction ferromagnetically. The bilinear exchange interaction parameter $J_z < 0$ favors the antiferromagnetic alignment of the spins. The temperature competes with all these parameters to destroy all possible orders, i.e., it forces the spins to orient themselves randomly leading to the paramagnetic phase. Δ_m leads to spin-canting which is a special condition which occurs

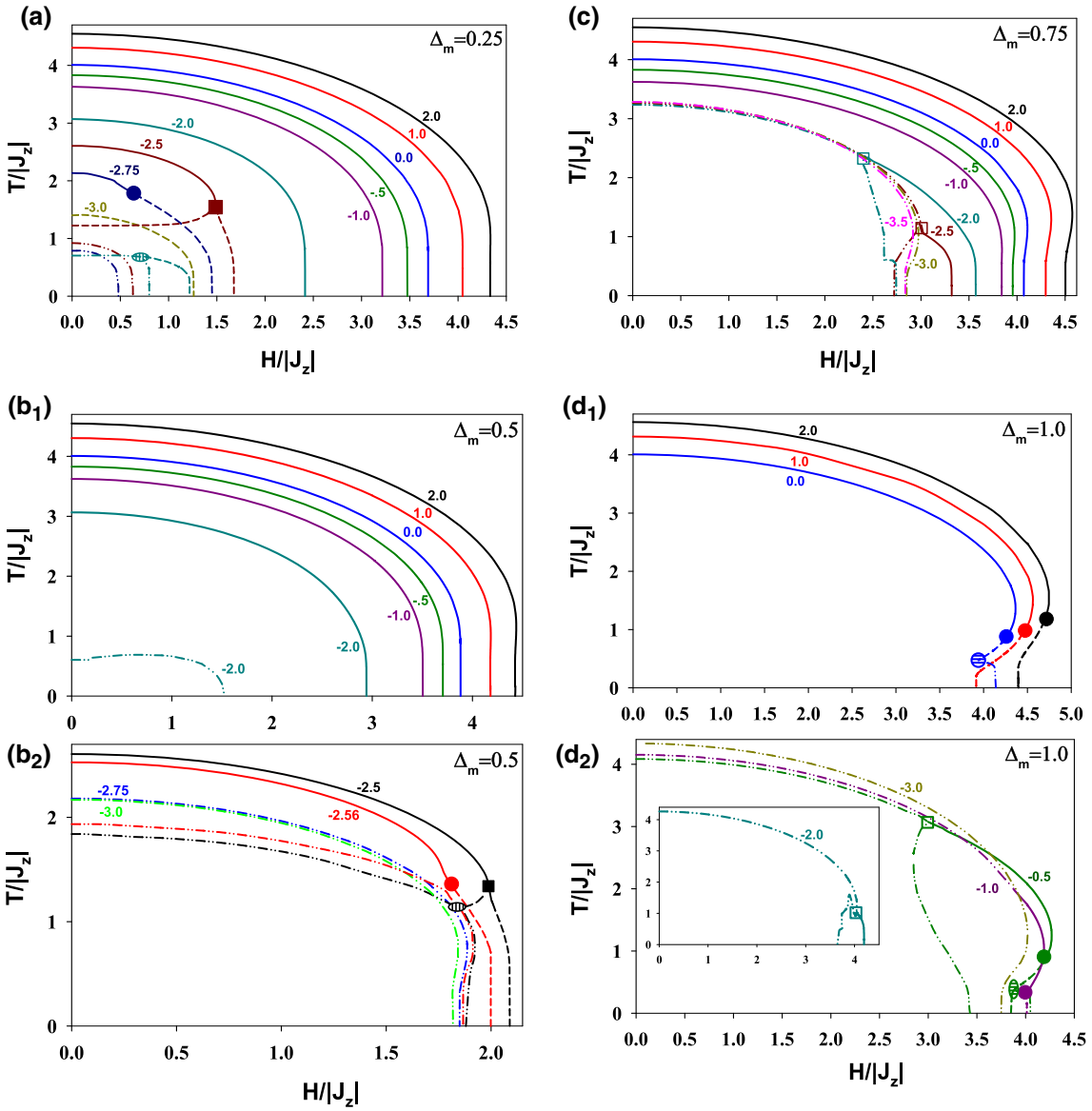

Fig. 2 The phase diagrams on the $(H/|J_z|, T/|J_z|)$ planes for given values of D_z when **a** $\Delta_m = 0.25$, $\mathbf{b}_1$–$\mathbf{b}_2$ $\Delta_m = 0.5$, **c** $\Delta_m = 0.75$ and $\mathbf{d}_1$–$\mathbf{d}_2$ $\Delta_m = 1.0$

when antiparallel magnetic moments are deflected from the antiferromagnetic plane, resulting in a weak net magnetism. All these competitions should lead to very rich magnetic phase diagrams with various phase transitions and critical points.

The first phase diagrams are obtained on the $(H/|J_z|, T/|J_z|)$ planes for given values of D_z when $\Delta_m = 0.25, 0.5, 0.75$ and 1.0. Figure 2a is mapped for $\Delta_m = 0.25$ shows that the T_c-lines start from higher temperatures for higher D_z at $H = 0.0$ and they are lowered as H increases which eventually terminate at higher H for higher D_z. The T_t- and T_r-lines are seen at lower H and temperatures for negative D_z. It is clear that $T_c > T_t > T_r$ and the magnetic fields satisfy for each phase $H_c > H_t > H_r$. When $D_z = -2.0$, in addition to the T_c-line we see a combination T_t- and T_r-lines combined at the CEP_3 for low T and H values. For $D_z = -2.5$ the T_c- and T_t-lines unite at the BCP_1. The critical line is only T_t type for $D_z = -3.0$. The next one, Fig. 2b_1–b_2 is obtained for $\Delta_m = 0.5$. The first one shows that only the T_c-lines exist for $-1.0 \leq D_z \leq 2.0$. When $D_z = -2.0$, the T_r-line is also seen at low H and T in addition to T_c-line at higher H and T. The latter exhibits not only the BCP_1 but also the CEP_3 for $D_z = -2.5$. The lower portion of the T_t-line for $\Delta_m = 0.25$ is now turned into a T_r-line for $\Delta_m = 0.5$. For $D_z = -2.56$, one sees two separated lines with T_c- and T_t-lines combined at TCP_1 and only a T_r-line. The lines are only the T_r-lines for other values of D_z. The reentrant behavior at higher H for all the T_r-lines is also clear. Figure 2c is obtained for $\Delta_m = 0.75$ shows again the T_c-lines exist from $D_z = 2.0$ to -1.0. The reentrant behavior is also seen for these T_c-lines except for -1.0. When $D_z = -2.0$ and -2.5 the BCP_2 is observed. Only the T_r-lines are seen when $D_z = -3.0$ and -3.5 which display reentrant behavior also. In Fig. 2d, we see that the T_c-lines terminate at TCP_1 for $D_z = 2.0$, 0.0 and 1.0, the T_t-line for 1.0 also merges with a T_r-line at TCP_3.

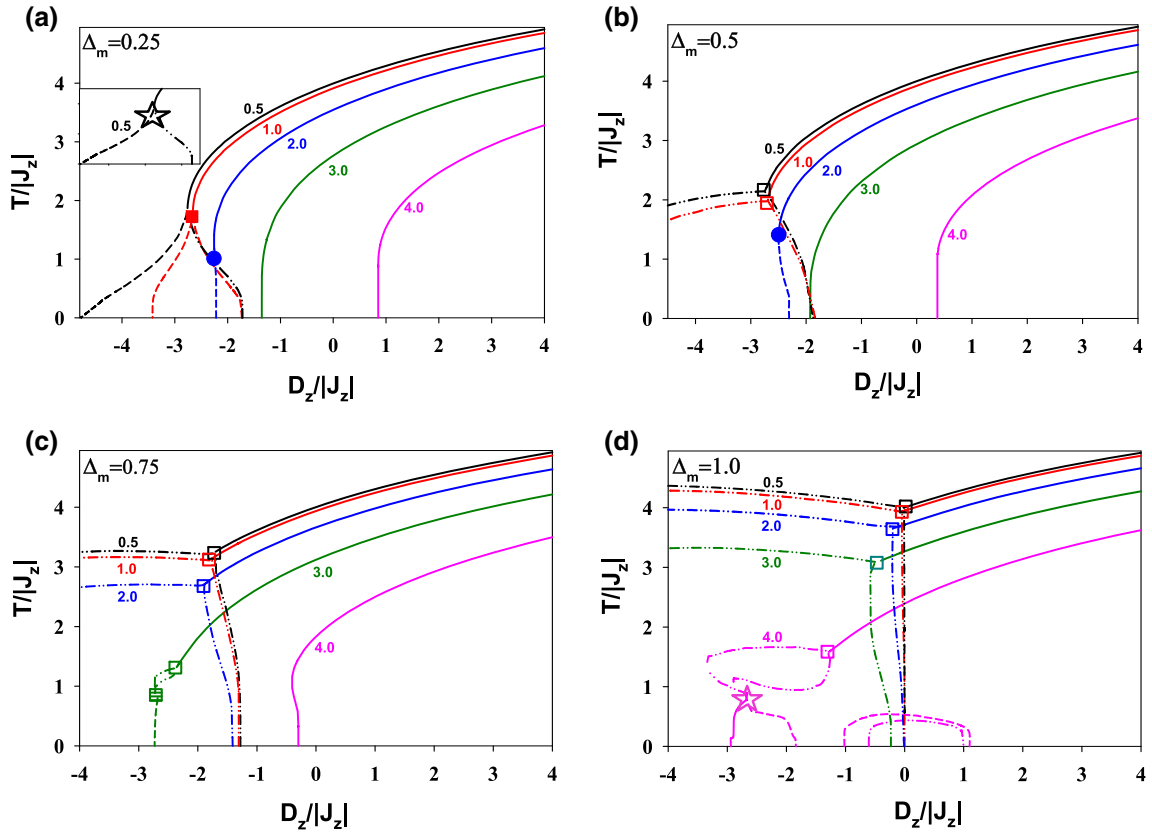

Fig. 3 The phase diagrams on the $(D_z/|J_z|, T/|J_z|)$ planes for given values of H when **a** $\Delta_m = 0.25$, **b** $\Delta_m = 0.5$, **c** $\Delta_m = 0.75$ and **d** $\Delta_m = 1.0$

For $D_z = -0.5$, we see all the phase lines with a BCP_2, a TCP_1 and CEP_3. When $D_z = -1.0$, we see TCP_1. BCP_2 is observed for $D_z = -2.0$. Again only a T_r-line is seen for $D_z = -3.0$. The T_c-lines always present some reentrant behavior. It is clear from these figures that as Δ_m increases the critical lines persist to higher H values.

The next phase diagrams are calculated on the $(D_z/|J_z|, T/|J_z|)$ planes for given values of H when $\Delta_m = 0.25$, 0.5, 0.75 and 1.0. Figure 3a is obtained for $\Delta_m = 0.25$. Only the T_c-lines are observed for $H = 3.0$ and 4.0 which start from lower D_z for lower H at zero T and they become constant temperature lines for higher D_z values. When $H = 2.0$, we see the combination of T_c- and T_t-lines combined at the TCP_1. The BCP_1 is seen for $H = 1.0$. The T_c-, T_t and T_r-lines emerge at the critical point indicated with a star for $H = 0.5$. For $\Delta_m = 0.5$, the T_c-lines for $H = 3.0$ and 4.0 moves to lower D_z values at zero temperature. This means increasing Δ_m shifts the T_c-lines to lower D_z. For $H = 2.0$, critical lines are the same as in Fig. 3b but now a bulging towards negative D_z values appears. The T_c- and T_r-lines combine at the BCP_2 for both $H = 0.5$ and 1.0. The case with $\Delta_m = 0.75$ is shown in Fig. 3c. Now for $H = 2.0$ we see that TCP_1 transforms into BCP_2. When $H = 3.0$, all types of the phase lines exit which are combined at BCP_2 and BCP_3. The bulging in T_c-line for $H = 4.0$ is also apparent. The last plot on this plane is calculated for $\Delta_m = 1.0$ exhibits BCP_2 for $H = 0.5 - 3.0$. Now $H = 4.0$ case is very complicated with half closed loops of T_t- and T_r-lines located around $D_z = 0.0$ as seen in Fig. 3d. The other parts of the critical lines consist of T_c-line terminating at BCP_2, then the T_r-lines enclose a region before combining and afterward the T_c-, T_t- and T_r-lines combine at the critical point indicated with the star.

The final phase diagrams, i.e., Fig. 4, are mapped on the $(\Delta_m/|J_z|, T/|J_z|)$ planes for given values of D_z when $H = 0.5$, 1.5, 3.0 and 4.0. In these figures, we always see the T_c-lines for $D_z = 2.0$ and 1.0 whatever the values of other parameters are. The temperatures of these lines decrease as H increases. They are not disturbed when H is small, i.e. for 0.5 and 1.5, since the T_c-lines stay straight. When $H = 3.0$, the temperatures of these lines are further lowered at small Δ_m values. They are further lowered when $H = 4.0$. Actually, $D_z = 1.0$ curve makes a deep at lower Δ_m but as Δ_m increases it's temperature rises. Thus, the magnetic field is strong enough to overcome when Δ_m is small but it eventually surrender to the effects of Δ_m. For $D_z = 0.0$ line we see that the T_c-lines behave as in the $D_z = 2.0$ and 1.0 cases. When $H = 4.0$, the T_c-line starts from zero temperature at about $\Delta_m = 0.63$, then rises as Δ_m increases. The T_t- and T_r-lines are also observed for higher Δ_m with $T_c > T_t > T_r$. The T_c-lines for $D_z = -1.0$ and -2.0 are similar with the previous T_c-lines, but now they terminate on their BCP_2's. For $D_z = -2.0$, we also see T_t-line merged together with the T_r-lines at BCP_3 for lower Δ_m. The case with $D_z = -3.0$ and -4.0 starts with the T_t-lines at nonzero temperatures then combine at the CEP_3 with their T_r-lines, which starts from zero temperatures at some mid-values of Δ_m and

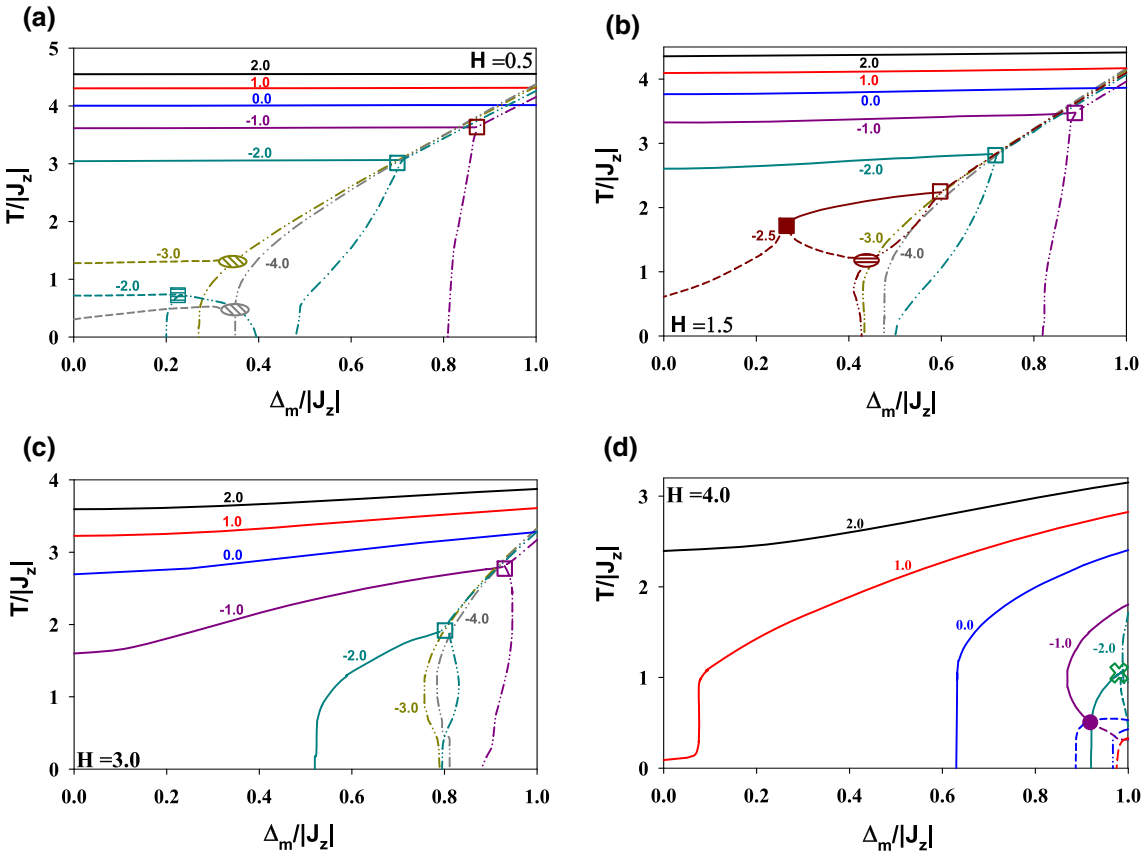

Fig. 4 The phase diagrams on the $(\Delta_m/|J_z|, T/|J_z|)$ planes for given values of H when **a** $H = 0.5$, **b** $H = 1.5$, **c** $H = 3.0$ and **d** $H = 4.0$

increase with increasing Δ_m. As H increases they move to higher Δ_m and disappear for $H = 4.0$. Figure 4b also shows the phase lines for $D_z = -2.5$ in which the T_r-lines are similar with the previous case. In addition, we see a T_c-line emerging from BCP_2 and terminating at the BCP_1. Then the T_t-line terminates on CEP_3. Finally, in the last figure we see the T_c- and T_t-lines combine at the TCP_1, the T_c- and T_t-lines terminate on the same point on a T_r-line indicated with a cross at higher Δ_m.

After having given all the details of the thermal variations of the net magnetization and the phase diagrams on possible planes, we are now ready to conclude this work in the last section.

5 Summary and conclusions

As a result of our investigation for the AFM spin-1 XYZ model by using a mean-field approach with the introduction of the spin operators on the model for the simple cubic lattice have revealed compelling behaviors for the total magnetization. It includes three different types of phase lines including the T_c-, T_t- and T_r-lines with three different phase regions, i.e., AFM, PM and random phase. In addition, various combinations of these lines have led to eleven types of critical points including the TCP, BCP and CEP, each of which are obtained in triples, and the critical points indicated with star and cross. The reentrant behavior was also observed in the T_c- and T_r-lines. It should be noted that negative crystal field values lead to interesting critical behaviors for our model as in the well-known Blume–Capel model. As we mentioned earlier as D_z becomes more negative the spin zero state of spin-1 is favored at lower temperatures. The external magnetic field tries to align the spins ferromagnetically by competing with D_z and with J_z, which favors AFM phase leading to zero magnetization, thus interesting critical behaviors are observed. It is also clear that as Δ_m increases toward the value of 1.0, the ordered phase regions move to higher magnetic field values as seen from the bulging of the phase lines which causes the existence of reentrant behavior. It should be noted that this is an approximate approach to the spin-1 XYZ model and it was inspired by the two-dimensional works mentioned in the references, thus, it only leaves us finding the eigenvalues of the model to calculate the partition function. This model has not been investigated so far; therefore, we cannot give any quantitative comparisons. As a last word, we hope that this work gets the attention of scientists for its deeper studies.

Acknowledgements This work was supported by the Research Fund of Erciyes University with Project Identification Number: FBA-2021-11571.

References

1. M.L. Néel, Ann. Phys. **12**, 137 (1948)
2. X.-Y. Gao, Y.-J. Guo, W.-R. Shan, Appl. Math. Lett. **120**, 107161 (2021)
3. M. Wang, B. Tian, C.-C. Hu, S.-H. Liu, Appl. Math. Lett. **119**, 106936 (2021)
4. Y. Shen, B. Tian, Appl. Math. Lett. **122**, 107301 (2021)
5. X.-Y. Gao, Y.-J. Guo, W.-R. Shan, Eur. Phys. J. Plus **136**, 893 (2021)
6. X.-Y. Gao, Y.-J. Guo, W.-R. Shan, Chaos Solitons Fract. **150**, 111066 (2021)
7. X.-T. Gao, B. Tian, Y. Shen, C.-H. Feng, Chaos Solitons Fract. **151**, 111222 (2021)
8. C.Z. Yang, J.L. Zhong, Phys. Stat. Sol. B **153**, 323 (1989)
9. J.L. Zhong, J.L. Li, C.Z. Yang, Phys. Stat. Sol. B **160**, 329 (1990)
10. M. Saber, J.W. Tucker, J. Magn. Magn. Mater. **102**, 287 (1991)
11. J.W. Tucker, J. Magn. Magn. Mater. **119**, 161 (1993)
12. J.P. Fittipaldi, E.F. Sarmento, T. Kaneyoshi, Physica A **186**, 591 (1992)
13. E.F. Sarmento, J.P. Fittipaldi, T. Kaneyoshi, J. Magn. Magn. Mater. **104–107**, 233 (1992)
14. X.F. Jiang, J.L. Li, J. Zhong, C.Z. Yang, Phys. Rev. B **47**, 827 (1993)
15. Y.Q. Ma, Y.G. Ma, C.D. Gong, Phys. Stat. Sol. B **177**, 215 (1993)
16. A. Benyoussef, H.E. Zahraouy, J. Phys. Condens. Matter **6**, 3411 (1994)
17. C.Z. Yang, W.J. Song, Phys. Stat. Sol. B **177**, K21 (1993)
18. E. Albayrak, Acta Phys. Pol. A **127**, 818 (2015)
19. E. Albayrak, Chin. Phys. B **22**, 077501 (2013)
20. E. Albayrak, Chin. Phys. Lett. **35**, 037501 (2018)
21. Q. Zhang, Y.W. Gu, G.Z. Wei, Proceedings of the third International Syposium on Magnenetic Industries (ISMI'04) and First International Symposium on Physical and IT Industries (ISITI'04) pp. 40–42 (2005)
22. E. Albayrak, M. Keskin, J. Magn. Magn. Mater. **206**, 83 (1999)
23. H. Ez-Zahraouy, H. Mahboub, M.J. Ouazzani, Int. J. Mod. Phys. B **18**, 4129 (2004)
24. J.R. Viana, O.D.R. Salmon, M.A. Neto, D.C. Carvalho, Int. J. Mod. Phys. B **32**, 1850038 (2018)
25. J. Ricardo de Sousa, F. Lacerda, I.P. Fittipaldi, Physica A **258**, 221 (1998)
26. G. Mert, J. Magn. Magn. Mater. **394**, 126 (2015)
27. A. Bobák, V. Pokorný, J. Dely, Physica A **388**, 2157 (2009)
28. A. Bobák, J. Dely, M. Žukovič, Physica A **390**, 1953 (2011)
29. A. Bobák, V. Pokorny, J. Dely, J. Phys. Conf. Ser. **200**, 022001 (2010)
30. A. Bobák, Z. Fecková, M. Žukovič, J. Magn. Magn. Mater. **323**, 813 (2011)
31. D.S. Takou, M. Karimou, F. Hontinfinde, E. Albayrak, Cond. Matter Phys. **24**, 13704 (2021)
32. E. Albayrak, Physica A **486**, 161 (2017)
33. E. Albayrak, J. Supercond. Nov. Magn. **30**, 2555 (2017)
34. J. Strečka, L. Čanová, J. Phys. Conf. Ser. **145**, 012012 (2009)
35. W.E.F. Parente, J.T.M. Pacobahyba, I.G. Araújo, M.A. Neto, J.R. de Sousa, Ü. Akinci, J. Magn. Magn. Mater. **355**, 235 (2014)
36. A.S. Freitas, D.F. de Albuquerque, Phys. Rev. E **91**, 012117 (2015)
37. G.-H. Liu, W.-L. You, W. Li, G. Su, J. Phys. Condens. Matter **27**, 165602 (2015)
38. A. Sera, Y. Kousaka, J. Akimitsu, M. Sera, T. Kawamata, Y. Koike, K. Inoue, Phys. Rev. B **94**, 214408 (2016)
39. Y.-H. Chan, W. Jin, H.-C. Jiang, O.A. Starykh, Phys. Rev. B **96**, 214441 (2017)
40. J. Strečka, L. Čanová, K. Minami, Phys. Rev. E **79**, 051103 (2009)
41. W.E.F. Parente, J.T.M. Pacobahyba, M.A. Neto, I.G. Araújo, J.A. Plascak, J. Magn. Magn. Mater. **462**, 8 (2018)
42. G.-H. Sun, X.-M. Kong, Physica A **370**, 585 (2006)
43. L.S. Lima, A.S.T. Pires, J. Magn. Magn. Mater. **320**, 2316 (2008)
44. G.-H. Liu, J.-Y. Dou, P. Lu, J. Magn. Magn. Mater. **401**, 796 (2016)
45. F.-Y. Li, G. Chen, Phys. Rev. B **98**, 045109 (2018)
46. H. Tschirhart, E.T.S. Ong, P. Sengupta, T.L. Schmidt, Phys. Rev. B **100**, 195111 (2019)
47. H. Komatsu, Y. Nonomura, M. Nishino, Phys. Rev. B **103**, 214404 (2021)
48. W.-N. Shi, F. Ming, D. Wang, L. Ye, Quantum Inf. Process. **18**, 70 (2019)
49. K.-H. Miitted, A. Schmidt, J. Phys. A Math. Gen. **28**, 2265 (1995)
50. C. Radhakrishnan, M. Parthasarathy, S. Jambulingam, T. Byrnes, Sci. Rep. **7**, 13865 (2017)
51. L.A. Takhtajan, Physica 3D **1–2**, 231 (1981)
52. E. Albayrak, Opt. Commun. **284**, 1631 (2011)
53. E. Albayrak, Eur. Phys. J. Plus, Submitted